FORTE – a multipurpose high-vacuum diffractometer for tender X-ray diffraction and spectroscopy at the SIRIUS beamline of Synchrotron SOLEIL

G. Ciatto, N. Aubert, M. Lecroard, C. Engblom, P. Fontaine, M. Dubuisson, M. Abiven, P.-E. Janolin, M. Kiat, Y. Dumont, et al.

FORTE - A multipurpose high vacuum diffractometer for tender x-ray diffraction and spectroscopy at the SIRIUS beamline of Synchrotron SOLEIL

G. Ciatto,[a]* N. Aubert,[a] M. Lecroard,[a] C. Engblom,[a] P. Fontaine,[a] J.-M Dubuisson,[a] Y.-M. Abiven,[a] P.-E. Janolin,[b] J.-M. Kiat,[b1] Y. Dumont,[c] B. Berini,[c] A. Fouchet[c2] and N. Keller[c]

[a]*Synchrotron SOLEIL, L'Orme des Merisiers, Saint-Aubin, BP 48 F-91192 Gif sur Yvette CEDEX France,* [b]*Laboratoire SPMS, UMR CNRS-CentraleSupélec, Bâtiment Gustave Eiffel - MB.105, 8-10 rue Joliot-Curie, 91190 Gif-Sur-Yvette CEDEX France, and* [c]*Groupe d'Etudes de la Matière Condensée (GEMaC), Université Versailles Saint-Quentin en Yvelines - CNRS, Université Paris-Saclay, Versailles France. E-mail: gianluca.ciatto@synchrotron-soleil.fr*

Abstract

A new high vacuum multipurpose diffractometer (called FORTE from the French acronyms of the project) has been recently installed at the tender/hard x-ray SIRIUS beamline of Synchrotron SOLEIL, France. The geometry chosen allows one to work either in the classical Eulerian four-circle geometry for bulk x-ray diffraction (XRD) or in the z-axis geometry for surface XRD. The diffractometer nicely fits the characteristics of the SIRIUS beamline, optimized to work in the 1.1 - 4.5 keV range,

[1] Deceased

[2] Present address: Laboratoire de Cristallographie et Sciences des Matériaux (CRISMAT), Université de Caen Normandie CNRS-ENSICAEN, Caen, France

and allows us to perform unprecedented diffraction anomalous fine structure (DAFS) experiments in the tender x-ray, also around non-specular reflections, covering large reciprocal space volume. Installation of a x-ray fluorescence detector on a dedicated flange allows simultaneous DAFS and x-ray absorption (XAS) measurements. The access to the tender x-ray opens the way to resonant investigations around the L-edges of second transition raw elements which are constituents of functional oxide materials. It also enables access to several edges of interest for semiconductors. Finally, the control architecture based on synchronized Delta-Tau units opens up exciting perspectives for improvement of the mechanical sphere of confusion.

1. Introduction

X-ray Diffraction (XRD) is still one of the most employed structural characterization techniques in synchrotron radiation facilities worldwide and free electron lasers; it applies to a variety of scientific area spanning from fundamental physics (McBride *et al.*, 2018) to biology (Nemoz *et al.*, 2018), from material science (Huang *et al.*, 2015) to cultural heritage (Bao *et al.*, 2018). On the one hand, the diversity in users' demand drove to the development of the most suitable instrumentation for specific applications, e.g. diffractometers with robotic sample changer systems and fast alignment tools for macromolecular crystallography beamlines (Fuchs *et al.*, 2014), many-circle diffractometers for precise alignment of crystals in materials science (Seeck *et al.*, 2012; Nowak *et al.*, 2006), ultra-high vacuum (UHV) instruments for reactive surface studies (Nicklin *et al.*, 2016; Fuoss & Robinson, 1984) and specific set-ups for liquids (Smilgies *et al.*, 2005; Murphy *et al.*, 2014; Fontaine *et al.*, 2014). Recently, the upgrade program that several synchrotrons have planned for lowering the emittance via the use of multi-bend achromat (MBA) storage rings (Einfeld, 2014) is boosting the design of diffractometers with sub-micron positional stability and reproducibil-

ity in order to benefit from the enhanced coherence of the future x-ray beams (Ju *et al.*, 2017). On the other hand, synchrotron beamlines often welcome different kind of experiments and sample environments, thus the versatility of the set up is also a very important criterion to be taken into account when building a diffractometer (Dyadkin *et al.*, 2016).

When working in the hard x-ray, absorption by air and windows is usually not a big issue in diffractometer design: the detector can be mounted out of the sample chamber (if any chamber exists), most of the positioning motors work in air reducing the risk of overheating and sample pollution, and space constraints are often less severe. Several geometries, using as many circles as necessary for the experimental applications, have been devised in order to cover the available reciprocal space (Bunk & Nielsen, 2004; Vlieg, 1998; Lohmeier & Vlieg, 1993; Thorkildsen *et al.*, 1999). Diffractometers hosting stations for in situ sample growth and characterization exploit the high brilliance and time structure of modern synchrotron radiation facilities (Lee *et al.*, 2016; Boichot *et al.*, 2016). However, in hard x-ray beamlines, due to the presence of beryllium (or other) windows and the use of double crystal monochromators equipped with Si crystals, the possibility to perform resonant scattering and diffraction below 3 keV is rare (Strempfer *et al.*, 2013).

In the soft x-ray, instead, absorption by the air is dramatic and the detector (with ultra-thin windows or windowless) has to inserted into the vacuum chamber. When the sample needs to be measured at low temperature, contamination is an issue because the sample can act as a cold finger in case of scarce vacuum level and contamination layers deposited on the sample surface can absorb an important fraction of the soft x-ray. This is the reason why several soft x-ray diffractometers/reflectometers were build by minimizing the number of in vacuum motors in order to reach UHV level. UHV is also necessary when the surface is sensitive and can react with residual water

vapors in the chamber; this is the case, for example, of ferroelectric oxides, where the dissociative adsorption of water can play as an extrinsic mechanism for screening the surface polarization charge. A typical strategy frequently exploited in soft x-ray beamlines was to choose an horizontal scattering geometry with sample actuation and detector rotation kept outside of the vacuum chamber, with the motion being transmitted through bellows and differential-pumped rotary seal (Jaouen *et al.*, 2004; Grabis *et al.*, 2003; Brück *et al.*, 2008; Staub *et al.*, 2008; Takeuchi *et al.*, 2009). These soft x-ray diffractometers/reflectometers are normally provided with an azimuthal angle (ϕ) covering a large range, either manual or motorized, and very limited (a few degrees) tilt angle (χ). Polarization is switched using the undulator source and without moving the sample. The degrees of freedom provided by this modified reflectometer geometry, considering also the strong contraction of reciprocal space in the soft x-ray, were sufficient to address the study of charge, magnetic and orbit ordering in several scientific cases, especially probing the magnetically active 3d electron band of first raw transation metals. In other soft x-rays reflectometers/diffractometers, a vertical scattering configuration was chosen to benefit from the low divergence of the beam (Beale *et al.*, 2010); in fewer examples the geometry featured in-vacuum motors (Hawthorn *et al.*, 2011; Beutier *et al.*, 2007) or aimed at integrating several experimental methods within the same sample environment (Abrudan *et al.*, 2015), sometimes compromising with the UHV vacuum level.

In the tender x-ray (arguably, the 1 - 5 keV range), the requirements of the hard x-ray and the issues intrinsic to the soft x-ray overlap: on the one hand the use of windows and (even) short sections in air is inconvenient due to the rather strong absorption; on the other hand several crystal plane reflections become available, depending on the material under study, and this calls for a larger covering of reciprocal space (i.e. a more extended range for the diffractometer circles) and better angular resolution to measure

the XRD peaks. Due to these difficulties, the tender x-ray energy range has been historically less exploited by XRD synchrotron beamlines worldwide, even for resonant studies. In addition, spectroscopy beamlines have often difficulties to cover the tender x-ray energy range too, being it located just between the two working ranges of application of classical grating and double crystal monochromators. Nevertheless, there is a tremendous interest in performing both resonant scattering/diffraction investigations and spectroscopy in the tender x-ray. In fact this energy range encompasses the L-edges of second transition raw elements (Sr, Y, Zr, Nb, Ru, Mo, etc.), which are constituents of functional oxide materials and also hosts several edges of interest for semiconductors (Al, Si, P, In, Sb, etc.).

In this paper we present a new multipurpose high vacuum (HV) diffractometer optimized to perform both XRD and spectroscopy in the tender x-ray. The HV diffractometer has been recently installed at the SIRIUS beamline of Synchrotron SOLEIL and showcases its innovative multilayer grating-based optics and undulator source. The design and geometry has been devised as a compromise among technical and users' requirements, versatility and vacuum level. This new end-station allows us to perform high quality diffraction anomalous fine structure (DAFS) experiments in the tender x-ray, also around non-specular reflections, covering large reciprocal space volume. It enables simultaneous DAFS and x-ray absorption (XAS) measurements in addition to resonant x-ray reflectivity (XRR) and tender x-ray grazing incidence small angle scattering (GISAXS). Moreover, the instrument will benefit from the characteristics of the upgraded SOLEIL ring for coherent diffraction imaging (CDI). The HV diffractometer was manufactured and assembled by the Symétrie company (Nîmes, France) and founded by two parallel projects: a joint agreement with the Swedish MAX IV Synchrotron (a twin prototype is under installation at the FemtoMAX beamline (Enquist *et al.*, 2018)) and a regional project, the Île-de-France DIM OXYMORE

project "FORTE" (from the French acronym), which also gave the name to the end station. In the next section we will give a brief recall of the main characteristics of the SIRIUS beamline; in Section 3 we will present the geometry, mechanics and performance of the diffractometer including available detectors, sample environment and control system; in Section 4 we will present selected results of the first commissioning and collaborative experiments performed with the end station; finally, in Section 5 we will draw a possible upgrade path for the next future before concluding.

2. The SIRIUS beamline

The SIRIUS beamline has been already described in two recent papers (Ciatto *et al.*, 2016; Fontaine *et al.*, 2014) and we remind to those references for a detailed presentation. Here, we limit to summarize the most important features that are key for the use of the FORTE diffractometer, which constitutes one of SIRIUS end-stations.

SIRIUS is mounted on an helicoidal Apple-II undulator x-ray source with 36mm magnetic period (HU36) (Kitegi *et al.*, 2010) which provides variable polarization (linear vertical, linear horizontal and circular) and it is equipped with two monochromators mounted in series and used alternately. The first is a double crystal monochromator (DCM) at a distance of 18.5 m from the source using a pair of liquid nitrogen-cooled Si [111] crystals; the second is a multilayer-grating monochromator (MGM) consisting of a variable line spaced holographic diffraction grating with line density = 2400 lines/mm over which a multilayer with 35 periods of Cr (2.5 nm)/B_4C (4.1 nm) has been deposited, and two matched multilayer mirrors as second optical element. The two monochromators are followed by a set of four mirrors which provide high harmonics rejection, focusing of the beam in the vertical and horizontal plane, and optional beam deflection. The smallest beam spot on the sample at the end-stations in focused mode (without flux reduction) is about 0.1 x 0.05 mm^2 (V x H) and four

positions of the beam at the end station level are possible according to whether the mirrors are used or not and to the specific mirror combination used.

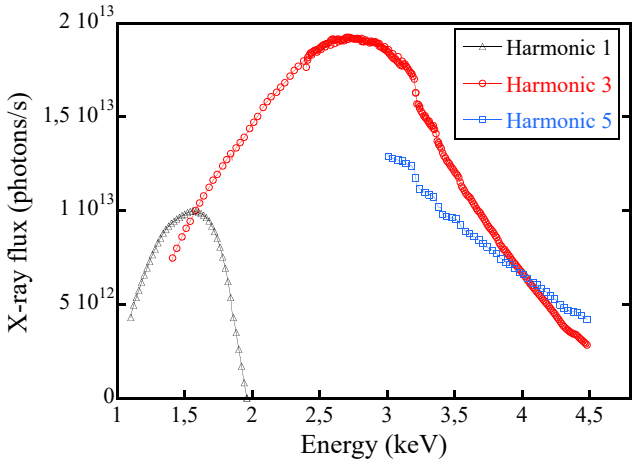

Fig. 1. X-ray flux impinging on the sample as a function of the energy in a typical configuration of the SIRIUS beamline using the MGM monochromator and the first three harmonics of the HU36 undulator.

Although the beamline provides photons in a continuous energy range 1.1 - 13 keV using either one or the other monochromator and it is routinely exploited also for hard x-ray studies, its range of excellence is the tender x-ray, where the MGM is used. This range matches the highest performance region of the SOLEIL ring. The MGM, which works in combination with an elliptic mirror focusing on a energy-selecting slit (ESS), provides high flux and good energy resolution in the 1.1 - 4.5 keV energy range. Moreover, it preserves circular polarization in this range, which would not be possible with the DCM being the Brewster angle for Si [111] located around 2.8 keV. As a consequence, the MGM can be also used for X-ray Magnetic Circular Dichroism (XMCD) and X-ray Resonant Magnetic Scattering (XRMS) experiments in the tender x-ray. The performances of the MGM are shown in Fig. 1 where the x-ray flux at the end station level is plotted as a function of energy for a typical high-energy-resolution configuration used for spectroscopy at grazing incidence. Here the beam is focused only vertically and the ESS is rather closed (5 μm); the x-ray flux

has been measured by using a ultra-thin optical grade diamond membrane specifically designed for monitoring the beam intensity/position and for normalizing spectra at the SIRIUS beamline (Desjardins *et al.*, 2014). Fig. 1 shows that, switching between the harmonics 1, 3 and 5 of the HU36 undulator, the x-ray flux can be maintained always above 4x10^{12} photons/s in the 1.1 - 4.5 keV energy range and it reaches almost the level of 2x10^{13} photons/s in the 2.5 - 3 keV range. Energy resolution (ΔE/E) is between 1.5x10^{-4} and 2x10^{-4} in the MGM energy range for the ESS opening chosen in Fig. 1, therefore close to the resolution offered by a Si[111] DCM and more than sufficient for application in XAS and DAFS spectroscopies. Flux can be raised above 3x10^{13} opening the ESS and accepting a lower energy resolution; such x-ray fluxes in the tender x-ray are rather impressive for a grating-based technology. More technical details about the MGM will be published in a dedicated paper currently in preparation.

The HV diffractometer that will be described in the following sections is one of the two end-stations available at the SIRIUS beamline; the other end-station is a large 7-circle diffractometer which can be used either with a "kappa head" goniometer (Thorkildsen *et al.*, 1999), on which a baby chamber can be mounted, or with a six-axis tower for heavy and cumbersome sample environments. Although there is no restriction in using the FORTE diffractometer also in the hard x-ray energy range up to 13 keV, the use of the other end-station is more convenient in that range. In fact, when the use of Be windows to separate vacuum and air sections does not represent a limit, the 7-circle diffractometer allows one to mount larger sample environments and detectors, to select longer sample-detector distances when necessary and to switch the samples faster.

3. The High Vacuum Diffractometer

3.1. Geometry

A conceptual sketch of the FORTE diffractometer geometry is shown in Fig. 2. The instrument consists of a four-circle Eulerian diffractometer with full range θ, δ, ϕ circles and a rather extended χ (more than 100 °) incorporated in a vacuum chamber, plus an additional vertical axis rotation (α) of the whole vessel ($\pm$ 10 °). The latter rotation is external to the vacuum vessel, and the connection of the vessel to the beamline requires the use of a bellow which can withstand movements about the α arc. This choice allows one to work either in a classical four-circle geometry (Busing & Levy, 1967) for bulk XRD (Fig. 2a) or in a configuration similar to the z-axis geometry (Mati Bloch, 1985; Feidenhans'l, 1989) for surface XRD, with the second detector circle replaced by a position sensitive detector (PSD) mounted on the δ arm. In the latter configuration (Fig. 2b), the sample surface is vertical (χ = 90 °), α is used to set (or scan) the incidence angle and a precise alignment of the sample surface normal with the ϕ rotation axis is possible by using an in vacuum hexapod mounted on the ϕ circle.

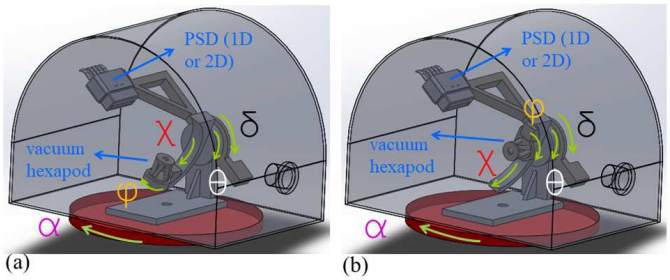

Fig. 2. Sketch of the HV diffractometer geometry. (a) four-circle configuration for bulk XRD; (b) configuration for surface XRD.

This geometry choice offers the following advantages:

- The absence of Be windows allows direct connection to the storage ring vacuum, enabling experiments down to energy as low as 1.1 keV.

- The use of a very open χ circle, analogously to a kappa geometry, leaves enough space on the side opposite to the mechanics for the installation of ancillary instrumentation (e. g., fluorescence x-ray detectors).
- The χ range is sufficiently wide to allow access to non-specular reflections which would not be accessible in a reflectometer geometry. To give an idea of the reciprocal space volume covered, in table 1 we show the list of the crystal place reflections reachable in resonant conditions for two case studies: a strained $In_{0.38}Ga_{0.62}As$ semiconductor pseudomorphic on GaAs substrate (tetragonal distortion of a zinc blende cell) analyzed at the In L3-edge, and a $PbSc_{0.5}Nb_{0.5}O_3$ relaxor oxide (trigonal, but approximable as a cubic perovskite) studied at the Nb L3-edge. The two edges are located in the tender x-ray, at 3.730 keV and 2.371 keV, respectively.
- The possibility to work either in vertical or horizontal scattering geometry provides high versatility in addressing the different users' demands. In particular, FORTE allows the use of grazing incidence x-ray diffraction, which has been demonstrated to be an unique tool in the study of thin films and nanostructures (Pietsch *et al.*, 2004), where it is important to reduce the background coming from the substrate scattering.

Moreover, the choice complied with space and weight constraints related with the installation in a rather narrow experimental hutch along with easy transport and maintenance.

Table 1. *List of the crystal plane reflections available in resonant conditions on two case studies (strained $In_{0.38}Ga_{0.62}As$ at the In L3-edge and $PbSc_{0.5}Nb_{0.5}O_3$ at the Nb L3-edge) given the diffractometer geometry shown in the sketch of Fig. 2. For each reflection, identified by the HKL Miller indexes, we include the corresponding δ and χ angles, the inter-plane spacing (d) and the momentum transfer ($Q = 2\pi/d$).*

$In_{0.38}Ga_{0.62}As$, In L3-edge (3.730 keV)

H	K	L	δ (degrees)	χ (degrees)	d (Å)	Q (Å^{-1})
1	0	1	47.83	46.49	4.10	1.53
1	1	0	49.13	90.00	4.00	1.57
0	0	2	67.86	0.00	2.98	2.11
2	0	0	72.03	90.00	2.83	2.22
1	1	2	88.22	36.68	2.39	2.62
2	1	1	91.15	66.99	2.33	2.70
2	0	2	108.34	46.49	2.05	3.07
2	2	0	112.51	90.00	2.00	3.14
1	0	3	125.10	19.35	1.87	3.36
3	0	1	135.36	72.44	1.80	3.49
3	1	0	136.77	90.00	1.79	3.51

$PbSc_{0.5}Nb_{0.5}O_3$, Nb L3-edge (2.371 keV)

H	K	L	δ (degrees)	χ (degrees)	d (Å)	Q (Å^{-1})
1	0	0	37.38	90.00	8.16	0.77
0	0	1	37.38	0.00	8.16	0.77
1	1	0	53.89	90.00	5.77	1.09
0	1	1	53.89	45.00	5.77	1.09
1	1	1	67.42	54.74	4.71	1.33
2	0	0	79.71	90.00	4.08	1.54
0	0	2	79.71	0.00	4.08	1.54
2	1	0	91.53	90.00	3.65	1.72
2	1	1	103.42	65.91	3.33	1.89
2	2	0	129.99	90.00	2.89	2.17
3	0	0	148.00	90.00	2.72	2.31
2	2	1	148.00	70.53	2.72	2.31

3.2. Mechanics and Performance

The conceptual sketch of Fig. 2 was materialized as shown in Fig. 3a: the FORTE diffractometer consists of a four-circle HV assembly and of two hexapods. The first (large) hexapod works in air, holding the entire vacuum vessel. Its vertical axis rotation (Rz) provides the α arc of the sketch ($\pm$ 10 deg), while the other five degrees of freedom are used to align the diffractometer and center it on the different possible positions of the incident beam, depending on the mirror configuration chosen. The second (small)

hexapod works under vacuum, mounted on the ϕ circle of the goniometer and bears the sample environments allowing at the same time a fine alignment of the sample surface, independent of the goniometer circles. The volume occupied by the end-station once the vacuum vessel is mounted, as shown in Fig. 3b, is 1499 x 1261 x 2176 mm^3 (LxWxH): the geometry chosen allowed us to limit the base projection, which was an issue for installation in a already existing experimental hutch. Total weight of the end-station is about 2050 Kg. When the end-station is used for grazing incidence x-ray diffraction, the entry flange is connected to the beamline by means of a large custom race track bellow with (internal) section = 372 x 70 mm^2 and length around 700 mm. The race track bellow, provided by Mewasa (Wangs, Switzerland), allows rotation of the whole diffractometer about the α vertical rotation axis along with wide translations in the three directions.

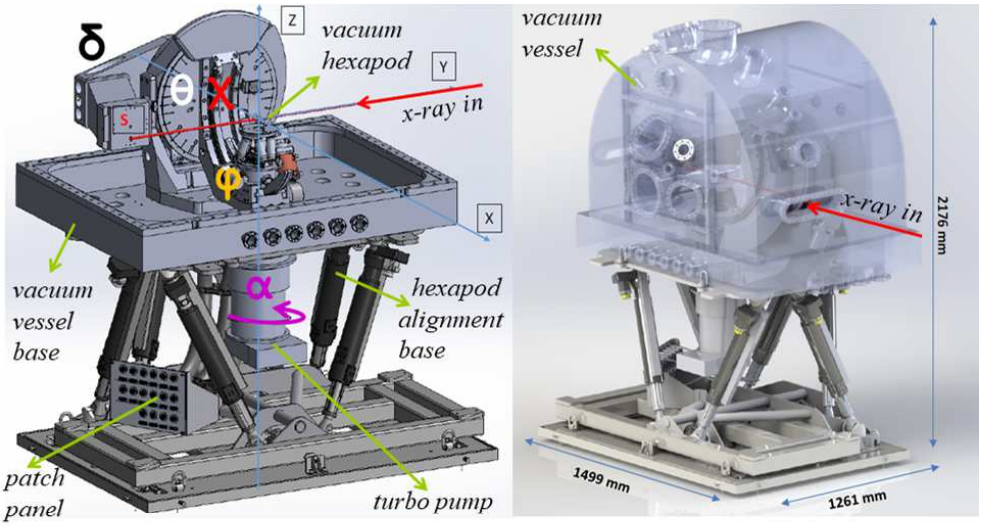

Fig. 3. (a) Illustration of the FORTE diffractometer showing its three main components: the four-circle HV assembly, the large air hexapod alignment base (JORAN) and the HV hexapod sample holder (BORA). (b) Illustration of the diffractometer including a sketch of the vacuum vessel showing the volume occupied by the end-station.

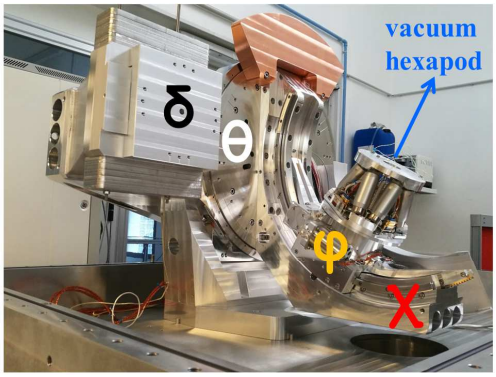

Fig. 4. The four-circle assembly based on Huber HV circles with the BORA hexapod mounted on the ϕ circle.

The four-circle diffractometer consists of HV compatible Huber (Rimsting, Germany) circles (Ref. 440.HV for θ; Ref. 411-X2W2.HV for δ, 5202.80.HV for χ and 410-X2W1.HV for ϕ). The circles are actuated by Phytron (Gröbenzell, Germany) HV compatible stepper motors equipped with Renishaw (Kingswood, UK) absolute encoders. Fig. 4 shows a photograph of the four-circle assembly; the mass of the assembly is 321 Kg, and the δ arm is optimized for a maximum payload of 12 Kg. The large base hexapod is a customized version of the JORAN hexapod manufactured by the Symétrie company (Nîmes, France); it uses stepper motors and absolute encoders for precision positioning. The possibility of aligning the diffractometer on the different possible beam positions (Ciatto *et al.*, 2016), which are rather distant both along the vertical axis (z) and along the axis transverse to the beam (x) when focusing mirrors are used, relies on the wide translation range allowed by JORAN (70 mm in z and 200 mm in x). The mass of JORAN is 335 Kg and its maximum payload permits to support diffractometer, vessel and ancillary instrumentation. The small vacuum hexapod is a standard HV compatible model (BORA) fabricated by the Symétrie company, featuring direct current (DC) motors and incremental encoders. Despite its small dimension (base diameter = 210 mm, height 141 mm) and mass (4.3 Kg), BORA

can withstand a maximum payload of 3.5 Kg in any direction; this feature, in addition with the location of the center of rotation of the two hexapod tilts 40 mm above the upper plate, allows the installation of different sample environments.

In order to manage the cables when the HV hexapod moves on the rotatory ϕ plate, a slip ring was installed along the ϕ axis of the goniometer taking advantage of the open base of BORA. The slip ring was manufactured by the RUAG company (Berne, Suisse). In addition to the hexapod actuator and encoder cables, the slip ring has eight free tracks that can be used for managing sample environment cables, including cables for sample heating, temperature and current measurements, electric field and polarization. Sample environment tracks are centralized into two D-Sub9 connectors fixed on the base of the BORA hexapod. A cable managing tool consisting in a stainless steel blade guided by an Al housing allows the ϕ + BORA subset to move along the 100 $^\circ$ of the χ circle segment; the housing maintains the blade when rotating θ. Outside the vacuum vessel, the cables coming from the vessel feedthroughs, along with the air JORAN cables, are guided via drag chains to a centralized patch panel installed on the JORAN base. Thanks to lifting eyes installed on the base and upper part of the vacuum vessel and to the customized JORAN base interface, the diffractometer can be easily removed from SIRIUS experimental hutch as an ensemble and stocked in a workshop or laboratory for maintenance and test; reproducibility of the montage is guaranteed by several alignment tools.

Table 2. *Measured parameters of the FORTE diffractometer.*

Axis	Range	Repeatability	Resolution	Precision	Speed
		Huber four-circle			
θ	± 180 °	0.0006 °	0.0002 °	0.0006 °	1 °/s
δ	-10 ÷ +180 °	0.0010 °	0.0002 °	0.0010 °	2 °/s
χ	-3 ÷ +100 °	0.0007 °	0.0002 °	0.0009 °	0.5 °/s
ϕ	± 180 °	0.0016 °	0.0002 °	0.0021 °	0.37 °/s
		JORAN hexapod			
α (Rz)	± 10 °	0.0003 °	0.0002 °	0.0006 °	0.17 °/s
Tz	-40 ÷ +30 mm	0.001 mm	0.001 mm	0.006 mm	0.93 mm/s
Tx	-95 ÷ +105 mm	0.001 mm	0.001 mm	0.016 mm	2.43 mm/s
Rx	± 2 °	0.0002 °	0.0002 °	0.0018 °	0.09 °/s
Ry	± 2 °	0.0002 °	0.0002 °	0.009 °	0.09 °/s
		BORA hexapod			
Tz	± 10 mm	0.0001 mm	0.0001 mm	0.0037 mm	1.1 mm/s
Tx	± 20 mm	0.0008 mm	0.0001 mm	0.013 mm	2.0 mm/s
Ty	± 20 mm	0.0007 mm	0.0001 mm	0.0107 mm	2.0 mm/s
Rx	± 10 °	0.0002 °	0.0001 °	0.0079 °	1.63 °/s
Ry	± 10 °	0.0001 °	0.0001 °	0.0059 °	1.88 °/s

The main performance parameters for all diffractometer axes are shown in table 2. In the table, as also shown in Fig. 3b, "z" represents the vertical direction; "y" the direction along the x-ray beam and "x" the direction in the horizontal plane perpendicular to y. "Tz" indicates a translation along the z axis and "Rz" a rotation about the z axis, the same meaning when switching z with x or y. It is worth remarking the wide angular range of the four-circle axes and of JORAN Tx and Tz, the very good repeatability of all axes on the full range of the movements (about 0.001 ° or better for angles and 1 μm or better for translations), and the excellent resolutions. As concerns the movement speed, this is relatively high for the θ, δ and BORA axes, and lower for the χ and ϕ axes due to space/mechanical constraints which drove the choice of the motors. JORAN Rx and Ry have also low speed: since these rotations are usually operated during the alignment phase and not frequently, we chose to favor repeatability versus speed. Even if no data acquisition is normally performed in our experiments during the hexapod movements, nevertheless care was taken in minimizing the cross coupling while an hexapod axis is operated. The sphere of confusion (SOC) of the

diffractometer was measured by using a metrology sphere of mass 3.5 Kg mounted on the BORA hexapod (the mass corresponds to BORA maximum load) and an Orbit digital lever probe by Solartron (Leicester, UK) fixed on the δ arm. The δ arm was also charged up to its maximum payload (12 Kg) for the measurement. SOC of the diffractometer (including the α arc) was found to be ≤ 100 μm at full charge and over the full extension of the diffractometer circles. This SOC value was found to be more than sufficient for all the experiments run until now and it is reasonable considering the present minimum beam size available at SIRIUS. In order to perform experiments with a smaller beam in the future (a few micron size) the SOC could be reduced considering that it mainly comes from systematic errors due to the χ circle guiding and flexion, and exploiting the electronics architecture described below in section 3.5.

3.3. Vacuum vessel and pumping system

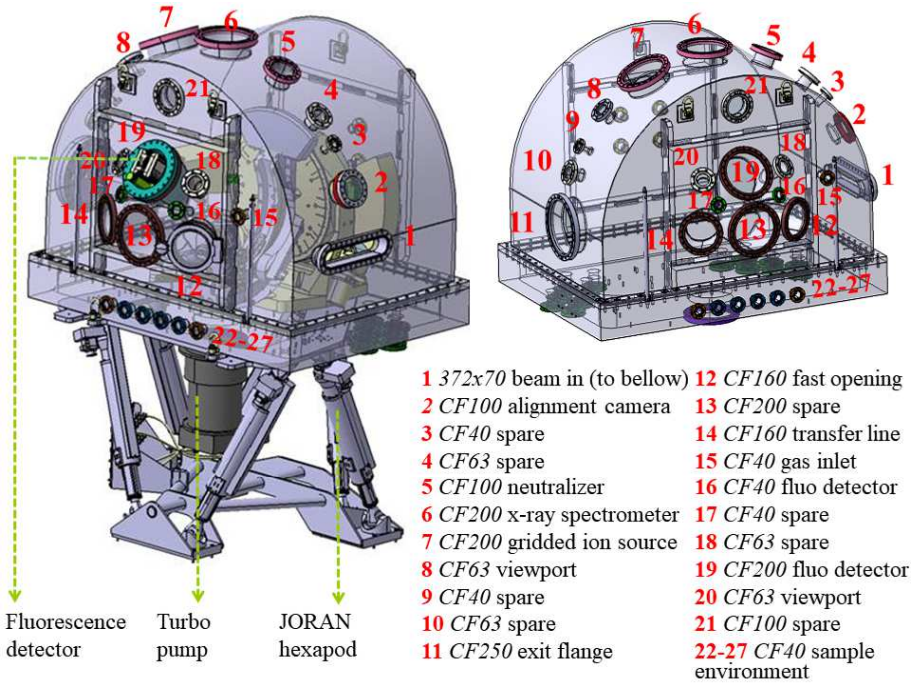

Fig. 5. Illustration of the FORTE vacuum vessel including list of the 27 frontal and top flanges. Other 19 flanges (not included in the list) are located in the rear and bottom sides of the vessel and are dedicated to the electrical feedthroughs of the vacuum motor/encoder cables and of the sample environment/detector electronics, to the turbo pump port, vacuum gauges, and pressure safety valve.

The vacuum vessel was provided by the SDMS company (Saint-Romans, France) following a SOLEIL design. It consists of a rectangular base of mass = 700 Kg and of a half cylinder-shaped cloche of mass = 635 Kg, both fabricated in stainless steel following certificated procedure for HV compatibility. The airtightness of all welding was certified as better than 10^{-8} mbar.l/s and verified via He leak tests. Fig. 5 shows illustrations of the vessel mounted on the JORAN diffractometer where all the 27 ConFlat (CF) flanges installed on the top/lateral and frontal sides of the vessel are shown; most flanges point to the diffractometer center i.e. to the sample position. Some of these flanges have been already used during the first experiments at SIRIUS, for example the custom flange 19 which allows insertion of a four-element silicon drift

detector (SDD) setting the nose at proximity of the sample. Flange 16 (interchangeable with 17) can be used to set a second SDD farer from the sample. Flange 12 is used to mount a viewport equipped with fast opening for manual access to the sample stage, while the in vacuum sample transfer line can be mounted on flange 14; these two flanges are interchangeable. Flanges 18 and 20, one of which is used to mount a viewport employed to visualize the sample during transfer, are interchangeable too. Flange 2 hosts an optical camera which also assists during sample change, the custom rectangular flange 1 is used for connection to the beamline vacuum trough the race track bellow described in section 3.2, and flange 27 for the electrical feedthrough for the heater described below in section 7. Other flanges are dedicated to the installation of new instrumentation in the short and middle term such as electrical feedthroughs and cooling lines for other sample environments (flanges 22-26), a gridded ion source (flange 7) with its neutralizer (flange 5) and a high-resolution vertical x-ray spectrometer (flange 6). Moreover, the diffractometer has been conceived as a versatile expandable platform and several other spare flanges have been added in order to meet new users' needs, equipments and ideas.

All the flanges used for the electrical feedthroughs of the vacuum motor/encoder cables and of the detector electronics, for the vacuum gauges, and pressure safety valves have been mounted either at the bottom of the chamber base or at the rear of the vacuum vessel. In fact, these 19 additional flanges do not need to be oriented towards the sample; moreover locating flanges out of the vessel cloche, when possible, make the opening of the vessel easier for maintenance and/or sample environment and detector change purposes. The flange (CF 200) for connecting a turbo-molecular pump is located at the bottom of the vessel base and allows installation of the pump between the legs of the JORAN hexapod without possibility of collision. We chose a ATH1603 M 200 turbo pump by Pfeiffer (Asslar, Germany) backed by a XDS35i

primary pump by Edwards (Burgess Hill, UK), the latter installed on a damper and far from the diffractometer to attenuate vibrations. This pumping system is sufficient to reach HV level: the diffractometer can pass from atmospheric pressure to the 10^{-7} mbar range in a few hours and to the 10^{-8} mbar range in a couple of weeks (if the chamber is not re-open) without the need of a bake out. This vacuum performance, obtained with the standard sample environment and detector inserted in the vessel (see section 3.4), is rather good considering the number of motors installed inside the vacuum vessel. The reachable vacuum level, sufficient for all the experiments carried out until now, could also be improved adding a second turbo pump on one of the flanges of the upper part of the vessel and/or performing a bake out of the chamber (the last procedure requiring the removal of sensitive instruments such as the four-element SDD). No issue related to vacuum motor overheating has been experienced until now, nevertheless the vessel base has been equipped with a flange reserved for a motor water cooling line in case of future need, and maximum temperature watch dogs have been set up.

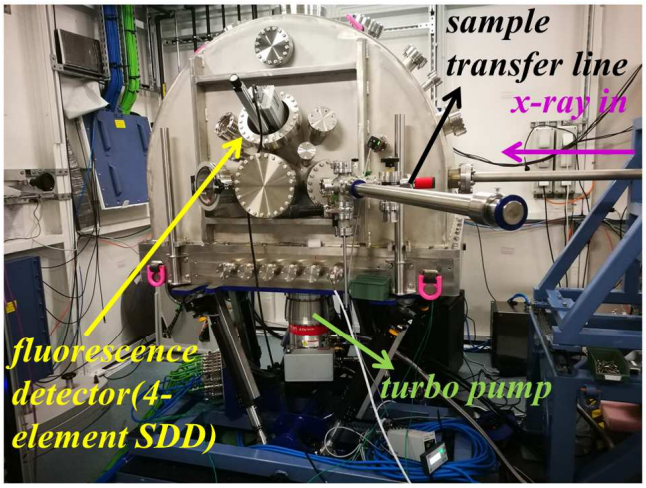

Fig. 6. Photograph of the FORTE diffractometer installed in the SIRIUS beamline experimental hutch.

Fig. 6 shows a photograph of the FORTE diffractometer installed in the SIRIUS

beamline experimental hutch with the turbo pump and fluorescence detector installed on the dedicated flanges. One can also remark, on the right side of the figure, the transfer line which allows sample change without breaking the vacuum. The in vacuum transfer line is based on a all metal sealed linear-rotary feedthrough equipped with rare earth magnets on the air- and vacuum side to provide the force to ensure a rigid coupling from the handle to the inner shaft. The sample transporter ends with a grabber tool suitable to manipulate flag style sample plates. The grabber has a matching slit to slide over the sample plate's handle, by twisting the grabber by 90° either way the sample plate can be either held by the grabber or released on a suitable receiver element. All the transfer line instrumentation is ultra-HV compatible and was provided by the Ferrovac company (Zürich, Switzerland). The transfer line is also equipped with a cross-shaped pre-chamber featuring a stage of four drawers for flag style sample plates; this allows one to transfer and measure four samples in a raw without opening the pre-chamber. Since the pre-chamber is separated from the main vessel and connected to an additional pump with suitable valves, opening of the main vessel is never needed except for sample environment and detector change.

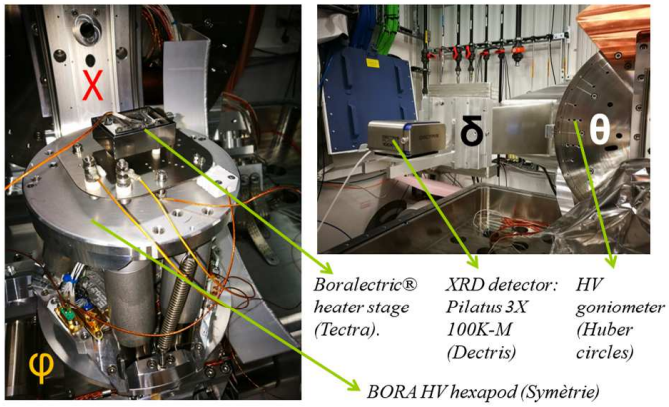

Fig. 7. Left: picture of the Boralectric heating stage mounted on the HV hexapod installed on the goniometer. Right: Pilatus3 100K-M detector mounted on the δ arm of the FORTE diffractometer.

The BORA hexapod can host a heating stage assembly provided by Tectra (Frankfurt, Germany), shown in Fig. 7 (left panel). The heating stage consists of a Boralectric heater (model HTR1001) equipped with twofold Nb foils for heat shielding and a type K thermocouple mounted inside the heater. It also includes a baseplate and threaded rods with hight adjustment, the latter used to position the sample surface at 40 mm from the BORA plate (i.e. the center of rotation of BORA Rx and Rz when the hexapod is on its reference position). A receiver for flag style sample plates by Ferrovac, fabricated in Mo for better performance at high temperature, is mounted on the Boralectric plate. The ϕ circle of the diffractometer and the BORA fine adjustments allow us to easily set the receiver in face of the the sample transporter mounted on its dedicated flange (see Fig. 6). All material and vacuum cabling comply with the HV standard. The heating stage, piloted by a PID-controller with autotuning, has been tested with positive results up to 700° during the diffractometer commissioning. No overheating of the BORA plate and other mechanics nor of the flanges where sensitive elements are located has been sensed. Exploiting the relatively large maximum payload

of the BORA hexapod (3.5 Kg), we plan to mount several other sample environments in the next future including a sample holder with electrical contacts for measurements under electric field and more precise temperature/current monitoring at the sample level, a cryostat, and a light variable magnetic field environment based on permanent magnets (Nolle *et al.*, 2012). This new instrumentation is presently under design.

The δ arm of the diffractometer allows the installation of several detectors with mass between 0 and 12 Kg, using a series of 12 counterweights of 1 Kg each for maintaining equilibrium. The detector that we use more frequently is a PILATUS3 100K-M two dimensional (2D) detector (Fig. 7, right panel) provided by Dectris (Baden, Switzerland). The detector has 172 x 172 μm^2 pixel size, a total detection area of 83.8 x 33.5 mm^2, and a 20 bits dynamic range; it can be positioned within a 160 - 517 mm distance range from the sample according to the experimental needs, thanks to a sliding support. PILATUS3 100K-M is designed with an HV compatible detector head which is inserted in the vessel, and a separated read-out electronics unit which is located outside (on one of the bottom flanges), the two elements being connected by a cable whose distance has to be kept smaller than 220 cm (including the electrical feedthrough). Nevertheless, this length allows complete covering of the δ circle angular range without any collision of the cables with the mechanics during movements. Water cooling of the detector head is assured by 250 cm long flexible hoses coupled with suitable cooling feedthroughs. We chose a detector with the ultra low energy calibration option, where the energy threshold can be adjusted between 1.6 and 18 keV; since the energy resolution of the threshold is 500 eV, the recommended working energy range starts around 2.0 - 2.1 keV and goes until (and beyond) the maximum energy available at SIRIUS. The use a robust, sensitive, and fast 2D detector is invaluable when performing grazing incidence XRD or tender x-ray small angle scattering (SAXS), however the PILATUS3 100K-M does not allow us to work down to 1.1 keV.

For energy < 2 keV, we presently use a point detector preceded by vacuum slits: the detector is a in-vacuum Peltier-cooled windowless Hamamatsu S2592-04 diode (Hamamatsu City, Japan) with high shunt resistance. The diode electronics consists of a FEMTO DDPCA-300 current amplifier coupled with analogical to digital converter (ADC) Adlink 2005 (500 kHz) with a 16 bit dynamics over 0-10 V. In parallel with the vacuum detectors for XRD, a Bruker XFlash QUAD 5040 four-element SDD fluorescence detector (Billerica, USA) is mounted on flange 19 (see Fig. 5 and 6) for XAS measurements; the detector is equipped with an 8 μm-thick Be vacuum window and it is coupled to a four-channel xMAP DXP electronics provided by XIA (Hayward, USA). Finally, the large PILATUS3 1M (Broennimann *et al.*, 2006) detector available at SIRIUS could also be connected to exit flange 11 (Fig. 5) for tender x-ray GISAXS experience in He environment.

3.5. Electronics, Software, and Control

The diffractometer subsystems (the JORAN and BORA hexapods, and the Huber four-circle assembly) utilize sixteen encoded motors to achieve six degrees-of-freedom (DOF) on diffractometer alignment, six DOF on sample alignment, and a total of five DOF on sample and detector rotations. Performing the necessary movements and/or alignments with low SOC values not only puts high constraints on the mechanical construction, but also on control system requirements. As such, the control system has been implemented using a pre-defined architecture from the REVOLUTION Project (Zhang *et al.*, 2015), here based on the high-performing Delta Tau Powerbrick controller which has been recently integrated as a SOLEIL standard. This controller offers, amongst many features, powerful processing capacity, multi-axis synchronization, encoder processing, virtual/operational space control through kinematic equations, and non-linear trajectories (Abiven *et al.*, 2017). In addition, TANGO

(http://www.tango-controls.org/) interfacing has been made possible using embedded software libraries written in-house at SOLEIL (Abiven *et al.*, 2017). FORTE control architecture has been developed thanks to a collaboration between SOLEIL, which has provided the high-level TANGO interface, and the Symétrie company, which has provided integrated kinematic routines and system configurations for the hexapods and four-circle subsystems (Abiven *et al.*, 2017) (see Fig. 8).

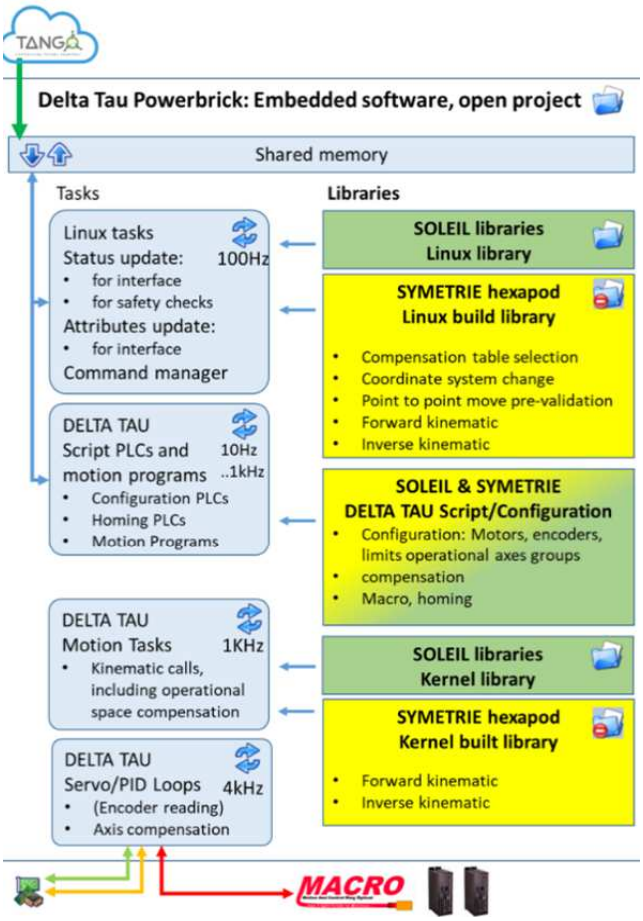

Fig. 8. Controller embedded software. In the SOLEIL-SYMETRIE collaboration, SOLEIL has provided TANGO interfacing libraries (marked green), while SYMETRIE has provided kinematic routines and system configurations (marked yellow).

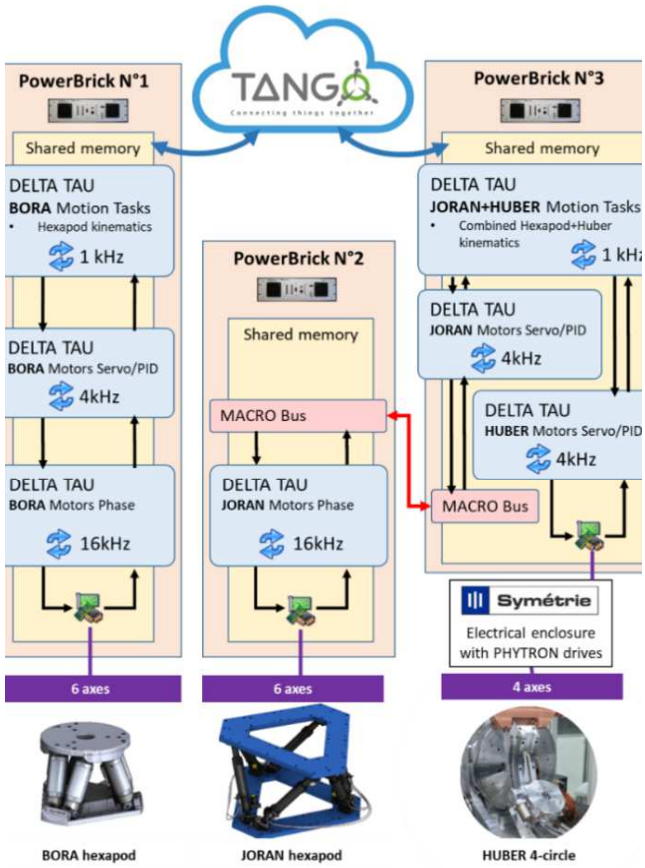

Fig. 9. Low-Level system control architecture.

The implemented architecture uses three Delta Tau Powerbrick LV IMS controllers each interfacing its own subsystem. The temperatures of the in-vacuum motors are also monitored by an external PLC which interlocks the motion controllers in case of overheating. Dedicated motor drivers (Phytron) are used for the Huber four-circle system. Figure 9 shows a more detailed overview of the low-level control architecture. Here, control is classified into two separate schemes:

A Powerbrick N 1 (BORA Control System, Multi-axial Cascaded control): All six motors are separately driven and controlled with motor phase currents at 16 kHz and motor positional servo control at 4 kHz; all of which move in synchronized

trajectories using model-based kinematics. TANGO control is exerted via the shared memory using dedicated libraries.

B Powerbrick N 3+2 (JORAN+Huber Control System, Multi-axial Cascaded control over 2 controllers): Synchronized control of the JORAN and Huber four-circle systems is achieved via the MACRO bus (an open protocol developed by Delta Tau that is used for real-time motion (Abiven *et al.*, 2017)) between two Powerbrick controllers. This allows the master controller (No. 3) to perform the closed-loop servo (at 4 kHz) and synchronized multi-axial trajectory calculations (with kinematics at 1 kHz) for the JORAN and Huber systems. TANGO control is exerted via the master controller. Synchronized motion of the Huber assembly and JORAN allows for two major advantages:

1. The JORAN platform can also be used for sample and detector movements, thus adding a 5th rotational DOF to the Huber four-circle system (the α angle defined in section 3.1).
2. Repeatable motion errors of the Huber four-circle assembly can be corrected for with the JORAN platform using compensation tables (in a feedforward manner), and thus reducing the SOC of detector and sample circular motions.

The second control scheme (B) works well when using six DOF hexapods for motion error compensation. This scheme can be further scaled up to synchronize all Powerbricks (No 1+2+3) using the MACRO Bus; this will allow the use of BORA hexapod (instead of JORAN) to improve the diffractometer SOC via compensation tables. The use of BORA for this purpose is more convenient since its movements are faster and they do not induce a displacement of the diffractometer center with respect to the incident beam position. These synchronization possibilities and the SOC improvement

will be key for future experiments with smaller x-ray beams (see section 5).

The TANGO control software can be further employed using a high-level environment developed at SOLEIL (called SPYC) that provides a friendly and versatile interface to the users. The SPYC platform is written in the Python programming language and allows one to use commands to move and scan several motors at the same time (undulator gap, monochromator and diffractometer axes), and to write scripts and macros for automatic acquisition.

4. Experimental applications

In this section we show selected examples of the results of the first commissioning and collaborative experiments very recently performed using the FORTE diffractometer, which was commissioned at the SIRIUS beamline in the first semester 2018 and it is nowadays open to the public user program. We present here data relative to tender x-ray DAFS experiments, tender x-ray grazing incidence XAS and XRD reciprocal space mapping. The use of the end-station for other experiments, such as tender x-ray SAXS/GISAXS and resonant XRR, is also possible and some of them are foreseen for the next future. It is worth remarking that this section exclusively aims at presenting the potential of the new HV diffractometer for experiments, while quantitative analysis of the results presented (which is presently in progress) is out of the scope of this manuscript.

4.1. Tender x-ray DAFS

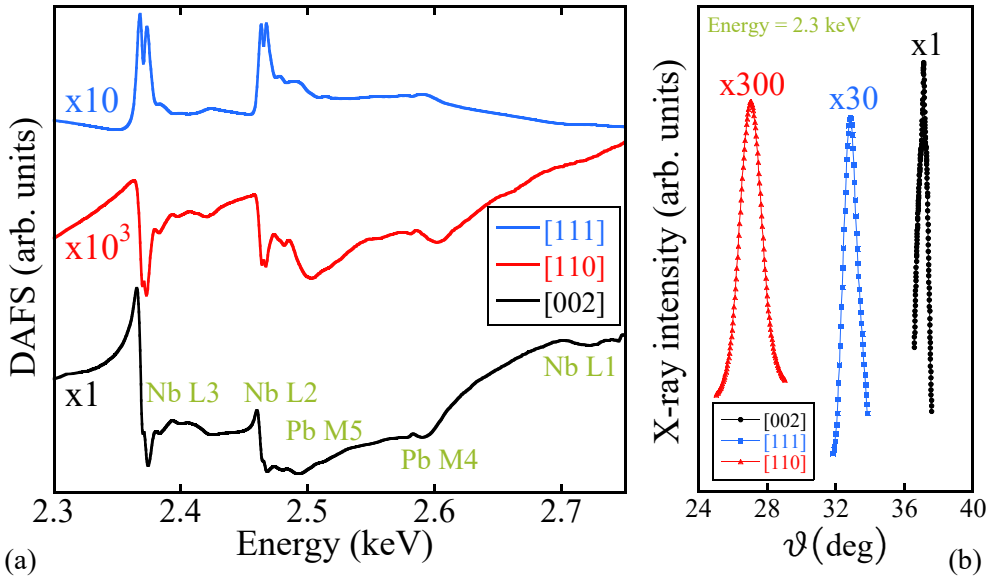

Fig. 10. (a) DAFS spectra taken on a $PbSc_{0.5}Nb_{0.5}O_3$ sample using three different reflections ([002], [110], [111]), spanning the energy range of the Nb L-edges and the Pb M-edges. The three DAFS spectra are multiplied by a factor (given in the left part of the figure) in order to be plotted on the same scale. (b) XRD θ-2θ scans performed around the three crystal plane reflections at energy = 2.3 keV.

$PbSc_{0.5}Nb_{0.5}O_3$ (PSN) is a perovskite oxide (ABO_3) whose proprieties switch from ferroelectric (FE) to relaxor or anti-ferroelectric according to the degree of ordering of Sc and Nb atoms on the B-site (FE when partially ordered, anti-FE when perfectly ordered and relaxor when disordered) (Malibert *et al.*, 1997). Correlated anti-parallel displacements of the Pb cations as well as oxygen octahedra rotations can influence the proprieties of the material, which is interesting for technological applications in filters, sensors/actuators, and antennas. Coexistence between ordered and disordered regions within the same sample is also possible. When these crystals are studied with x-ray diffraction, different reflections are visible: some of them are pure structural reflections (as the [002] one), others are superstructure reflections arising from the ordered alternation of Sc and Nb planes (as the [110] one), others again are thought to

reflect chemical order (Sc, Nb) along a crystallographic direction plus the anti-parallel cationic displacements along the same direction (as the [111] one). Fig. 10a shows three DAFS spectra taken using the [002], [110], and [111] reflections in an energy interval spanning the L-absorption edges of Nb and the M-edges of Pb; Fig. 10b shows XRD θ-2θ scans performed around the three crystal plane reflections at energy = 2.3 keV where the Bragg peaks are visible. Quantitative analysis of the DAFS spectra taken at the different structure and super-structure reflections will allow us to shade some light about the relative fraction and nature of the chemically ordered regions. In particular, DAFS is suitable to understand how the single elements participate to a specific super-structural order and if the local structure of the atoms involved in that super-structural order is different from the average one. Together with XAS data obtained at the Nb L-edges and Sc k-edge on the same samples (not shown), these experimental results will be very useful to clarify the correlation between short range order, local density of states and relaxor properties in PSN. We note here that the use of the Nb L3-edge makes our probe sensitive to orbitals with d-symmetry, which is particular important since Nb has 4d-electrons in the valence band and these electrons are involved in bonding with O 2p-electrons. Eventually, it is also worth remarking that the use of a four-circle diffractometer with large angular range (including for χ) is here mandatory to explore the different reflections used in the DAFS study (see table 1, bottom part).

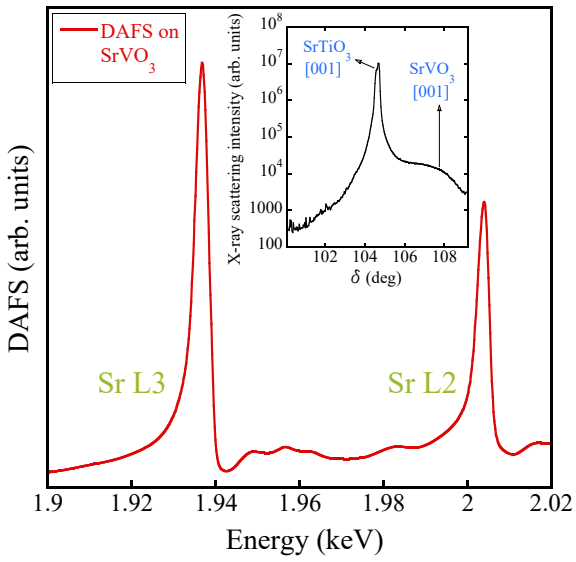

Fig. 11. Sr L3-edge DAFS spectrum of a 35 nm $SrVO_3$ layer sandwiched in a $LaAlO_3/SrVO_3/SrTiO_3$ structure; inset: XRD θ-2θ scan around the $SrTiO_3$ [001] substrate peak showing the $SrVO_3$ [001] shoulder on the high-angle side.

Another scientific case which can benefit from tender x-ray DAFS is the study of strong correlated functional oxide systems showing a metal-insulator transition (MIT). In $SrVO_3$ (SVO) (Yoshimatsu *et al.*, 2010; Gu *et al.*, 2014; Fouchet *et al.*, 2016; Fouchet *et al.*, 2018), which is a paramagnetic metal in the bulk, the MIT can be induced by decreasing the thickness to a few nanometers. Furthermore, the MIT can be influenced by the strain imposed to the thin epitaxial SVO layer by different kind of substrates such as a stressful $SrTiO_3$ (STO) or a more matching $(La,Sr)(Al,Ta)O_3$ (LSAT); the presence of a cap layer (STO or $LaAlO_3$, LAO) can also stress the metallic SVO layer. Hence, the study of the effects of under or upper strains on the local structure of all elements in the SVO layer is crucial to disentangle the pure dimensional reduction effect from strain effects in sandwiched SVO layers. It is highly relevant to correlate these effects with the electronic structure and transport properties. If on the one hand the local environment of V atoms (occupying the "B" site of the perovskite) can be accessed via XAS, on the other hand a study of the local structure and local

density of states around the Sr atoms (occupying the "A" site) as a function of the SVO layer thickness requires the combined chemical and crystallographic selectivity of DAFS, due to the presence of Sr in both STO and LSAT substrates. The use of grazing incidence (GI) XAS is not an option considering the presence of a nanometric cap layer. In Fig. 11 we show a DAFS spectrum of a LAO(3nm)/SVO(35nm)/STO heterostructure in the region of the Sr L3 and L2 absorption edges, selecting the [001] crystal plane reflection of SVO. As shown in Fig. 11 inset, the SVO [001] reflection can be separated as a shoulder on the right side of the intense STO [001] substrate peak in a XRD θ-2θ scan. The DAFS Sr L3-edge spectra have very high quality; simulating them *ab initio* based on model strain structures will be very helpful in monitoring and understanding the evolution of the Sr local density of unoccupied states and local structure as a function of the sample thickness, through the MIT transition. We note once more that access to the Sr L3 and L2 absorption edges is important because this allows us to probe final states with d-symmetry, relevant in the chemical bonds. Since these edges are located at rather low energies in the tender x-ray (1.94 and 2.0 keV), large δ angles (between 100 ° and 120 °) are necessary; the DAFS experiment is possible indeed thanks to the wide δ range made available by FORTE diffractometer. For uncapped samples, the SVO [100] reflection, accessible in GI, could also be used for DAFS thanks to the possibility to switch from bulk to surface geometry anticipated in section 3.1: choosing a GI-DAFS geometry would permit to enhance the diffraction signal of the SVO layer with respect to the substrate one.

4.2. Tender x-ray grazing incidence XAS

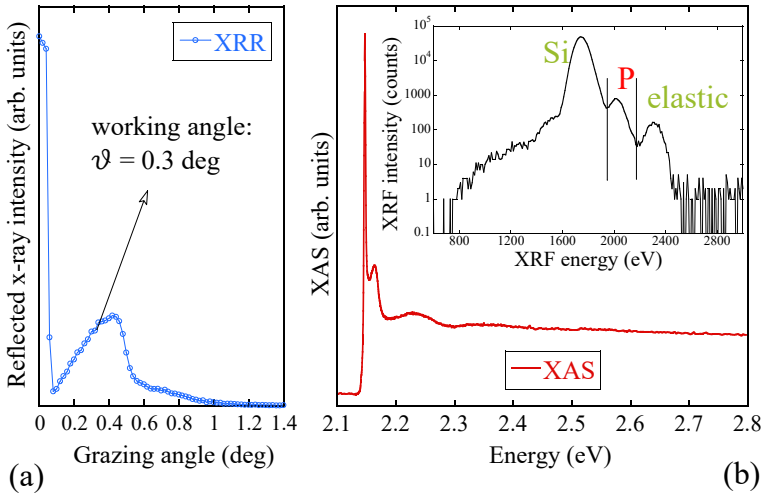

Fig. 12. (a) XRR curve in the vicinity of the P K-edge taken on a ODPA monolayer deposited on Si substrate. (b) P K-edge GI-XAS spectrum of the same sample taken in fluorescence mode with the SDD; the inset shows a fluorescence spectrum taken at 2.3 keV in GI, where it is possible to discriminate the P Kα peak from the Si Kα and elastic peaks.

In parallel to tender XRD and DAFS, FORTE diffractometer can also be used for XAS experiments in the same energy range, thanks to the four-element SDD described in section 3, which allows measurement of even ultra high dilute systems. In some cases, when the sample geometry and Bragg angles at play allow it and self-absorption is not an issue, XAS measurements can also be performed simultaneously to DAFS resulting in time saving (Ciatto *et al.*, 2018). In other cases, it may be interesting to choose a specific incidence angle for the XAS measurements; this is often a need in experiments on nanostructures, where confining the x-ray probe in a near-surface region using a subcritical grazing angle allows reduction of the signal background generated from fluorescence lines originating from the substrate or buffer layers. In Fig. 12 we present XRR and P K-edge XAS spectra taken on a self-assembled monolayer P-containing molecule, the octadecylphosphonic acid (ODPA), deposited on Si substrate. This molecule is interesting for the monolayer contact doping process of Si and

related nanostructures (Arduca *et al.*, 2016), in which a subsequent annealing forces P diffusion into the structure beneath the molecule; doping of nanostructured semiconductor is in fact a key issue for future nanoelectronics. As a prelimary information to the monolayer contact doping process, it is interesting to know the local structure of P in the as-deposited layers and the interaction and bonding with the Si substrate. A study of a the local environment of P by fluorescence mode XAS on this system is challenging since, even if the P Kα and Si Kα lines are separated by $\sim$ 300 eV and the energy resolution of SIRIUS SDD is $\sim$ 130 eV, the strong Si fluorescence background coming from the substrate would hinder any XAS measurements at the P K-edge in wide-incident angle geometry. In fact, the fluorescence detector would saturate before having a sufficiently high P Kα count rate. Using FORTE diffractometer, we can perform precise reflectivity curves to determinate the critical angle of the sample, using the HV PILATUS3 100K-M detector for measuring the reflected signal (Fig. 12a). Working at incidence angles smaller than the critical one for total reflection (we chose $\theta = 0.3\ ^\circ$ in this case) allows limitation of the x-ray penetration to a few nm beneath the surface, enhancing the monolayer contribution and improving the P/Si Kα count ratio and signal to noise. This setup allows us to separate the P Kα signal located between the Si Kα and elastic peaks in a fluorescence spectrum taken after the edge (Fig 12b inset), and to obtain from its integration high quality P K-edge XAS spectra of the deposited monolayer ODPA molecule (Fig 12b body).

4.3. Reciprocal Space Mapping

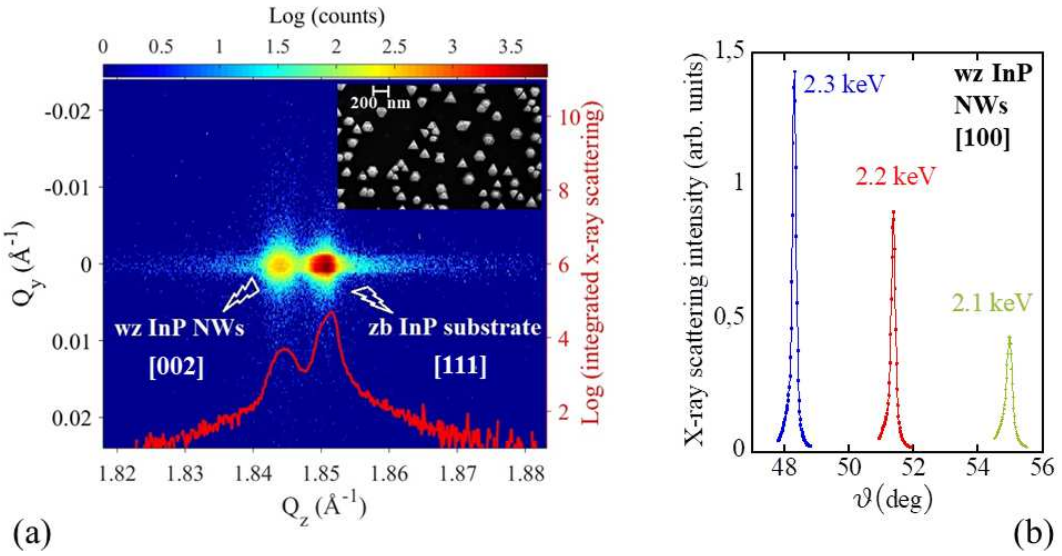

Fig. 13. (a) RSM taken at 2.2 keV on InP wz nanowires grown on InP zb substrate using the PILATUS3 100K-M detector. The close XRD spots of the wz [002] reflection and the zb [111] one can be separated in the map. A (red) curve representing the count rate integrated along the Q_y direction is superposed to the RSM. Q_y is the component of the momentum transfer in y direction (transversal to the x-ray beam), Q_z is the component perpendicular to the surface. The inset shows a SEM image of the sample. (b) XRD θ-2θ scans performed in GI around the [100] reflection of the InP wz nanowires for different energies around the P K-edge.

The availability of an in vacuum 2D detector mounted on the δ arm of the FORTE diffractometer opens the possibility of acquiring XRD reciprocal space maps (RSMs) in a fast way, in particular at energies corresponding to resonances of interest in the tender x-ray. RSMs are very useful to evaluate strain in epitaxial systems and can be associated to multiwavelength anomalous diffraction (MAD) (Hodeau *et al.*, 2001) to correlate specific strain regions with concentration gradients of the chemical elements (Létoublon *et al.*, 2004). Furthermore, in epitaxial templates, RSMs allow one to easily discriminate different diffraction peaks coming from the active layer, buffers and substrate, and to select the desired one for a DAFS analysis, even in case the same chemical element is present in more than one layer of the template. This is the

case shown in Fig. 13a, where we analyzed InP wurtzite (wz) [001] nanowires (NWs) grown on InP zincblende (zb) [111] substrate at an energy (2.2 keV) just above the P K-edge. Despite the low incidence energy, the wz [002] peak (δ = 112.07 °) and the [111] zb one (δ = 112.79 °) are still rather close from each other. Nevertheless, the reciprocal space map (RSM) of Fig. 13a allows separation of the two diffraction spots. Another strategy to discriminate the structure of the NWs from the substrate one is that of choosing the wz [100] reflection; this reflection (δ = 103.58 °) is accessible in grazing incidence using the FORTE configuration shown in Fig. 2b and, as one can see from the θ-2θ scans of Fig. 13b, has no substrate reflection immediately nearby.

5. Upgrade path

The upgrade path foreseen for the FORTE end-station will follow two lines. The first line consists in the aforementioned completion of the sample environment and detector set ups, beyond the basic functionality already implemented. This will include the installation of a sample holder with electrical contacts for measurements under electric field, interesting for the analysis of ferroelectric/piezoelectrics samples, a magnetic field environment for XMCD and XRMS measurements, a cryostat and, finally, a vertical high-resolution tender x-ray spectrometer with Von Hamos geometry (Anklamm *et al.*, 2014) for coupling XAS with X-ray Emission Spectroscopy (XES) in order to study the occupied/unoccupied local density of states and "local" band gaps in semiconductors (Amidani *et al.*, 2014).

The second line will go in parallel with the upgrade of SOLEIL ring towards a MBA lattice in the next future. The foreseen two orders of magnitude increase in brilliance will bring about an equivalent increase in the fraction of transverse coherence of the x-ray and, as consequence, of the coherent photon flux available at the beamlines. Moreover, in the case of SOLEIL ring, the performance improvement will be particu-

larly impressive in the tender x-ray region and for our kind of undulator source. This will pave the way for the use of FORTE end-station for coherent diffraction imaging (CDI) in Bragg geometry (Pfeifer *et al.*, 2006). It is worth remarking here that progress in the development of robust single photon counting 2D detectors working in the tender x-ray with pixel size smaller than in PILATUS (for example CMOS-based) is expected in the next future. These new detectors would prevent from having lower resolution in speckle sampling due to the limited maximum sample-detector distance and consequent reduced speckle size.

The possibility to use a smaller and intense x-ray beam will call for an improvement of the four-circle diffractometer SOC. The control architecture based on synchronized Delta-Tau units described in section 3.5 opens up exciting perspectives in this sense. In fact, since we know from the manufacturer that the SOC errors mainly origin from the χ circle guiding and flexion, a full metrology of these systematic errors could be carried out and the results injected as input in our control system to correct them in real time using synchronized movements of one of the hexapods (e.g., BORA).

6. Conclusions

We presented a high vacuum diffractometer for tender x-ray diffraction and spectroscopy recently installed at the SIRIUS beamline of the French national synchrotron source (synchrotron SOLEIL). This new end-station, called FORTE, is highly versatile and opens exciting perspectives to the users offering different techniques in the tender x-ray range: (GI)XRD, DAFS, (GI)XAS, XRR, GISAXS. The diffractometer allows investigation of bulk samples as well as of surfaces, interfaces and nanostructures; it has a sufficient number of circles and extended angular ranges to cover large volume in reciprocal space and can work in the 10^{-8} mbar vacuum range despite the presence of several in-vacuum motors. FORTE has been commissioned in the first semester

2018 and it is nowadays open to the public user program. Selected results of the first experiments performed have been shown as examples of its present potential. Finally, an appealing upgrade path of the end-station is foreseen in the next future.

Acknowledgements

We thank all the other colleagues at SOLEIL (in particular from the vacuum, alignment, detector, optics, electronics and software group) who gave a contribution to the conception and installation of the FORTE diffractometer. We thank the Symétrie company (Nîmes, France), and in particular O. Dupuy, for the excellent work in the design and assembly of the diffractometer system based on our conceptual idea. G. C. thanks P. Morin (SOLEIL) for advice during the project writing phase; J. Larsson (MAX IV) for useful discussion; H. Renevier, A. Deschampes (Grenoble-INP), and the SOLEIL Scientific Advisory Committee (SAC) for supporting the funds research. Finally, we thank M. De Luca (University of Basel), A. Polimeni (University of Rome La Sapienza), C. Jagadish (Australian National University), D. De Salvador and F. Sgarbossa (University of Padova) for providing some of the samples used in the experiments presented in the manuscript. The project was funded by the Swedish Research Council (Vetenskapsrådet MAX IV - SOLEIL collaboration) and the Île-de-France region (project "FORTE", DIM OXYMORE).

References

Abiven, Y. M., Aubert, N., Ciatto, G., Engblom, C., Fontaine, P., Zhang, S., L'Hostis, A., Noire, P., Dupuy, O. & Roux, T. (2017). In *Proceedings, 16th International Conference on Accelerator and Large Experimental Physics Control Systems (ICALEPCS 2017), Barcelona, Spain, Oct. 2017*, pp. 380–384.

Abrudan, R., Brüssing, F., Salikhov, R., Meermann, J., Radu, I., Ryll, H., Radu, F. & Zabel, H. (2015). *Rev. Sci. Instrum.* **86**, 063902.

Amidani, L., Ciatto, G., Boscherini, F., Filippone, F., Mattioli, G., Alippi, P., Bondino, F., Polimeni, A., Capizzi, M. & Amore Bonapasta, A. (2014). *Phys. Rev. B*, **89**, 085301.

Anklamm, L., Schlesiger, C., Malzer, W., Grötzsch, D., Neitzel, M. & Kanngießer, B. (2014). *Rev. Sci. Instrum.* **85**, 053110.

Arduca, E., Mastromatteo, M., De Salvador, D., Seguini, G., Lenardi, C., Napolitani, E. & Perego, M. (2016). *Nanotechnology*, **27**, 075606.

Bao, Y., Zhao, C., Li, Y. & Yun, X. (2018). *Scientific Reports*, **8**, 13523.

Beale, T. A. W., Hase, T. P. A., Iida, T., Endo, K., Steadman, P., Marshall, A. R., Dhesi, S. S., van der Laan, G. & Hatton, P. D. (2010). *Rev. Sci. Instrum.* **81**, 073904.

Beutier, G., Marty, A., Livet, F., van der Laan, G., Stanescu, S. & Bencok, P. (2007). *Rev. Sci. Instrum.* **78**, 093901.

Boichot, R., Tian, L., Richard, M. I., Crisci, A., Chaker, A., Cantelli, V., Coindeau, S., Lay, S., Ouled, T., Guichet, C., Chu, M. H., Aubert, N., Ciatto, G., Blanquet, E., Thomas, O., Deschanvres, J. L., Fong, D. D. & Renevier, H. (2016). *Chem. Mater.* **28**, 592.

Broennimann, C., Eikenberry, E. F., Henrich, B., Horisberger, R., Huelsen, G., Pohl, E., Schmitt, B., Schulze-Briese, C., Suzuki, M., Tomizaki, T., Toyokawa, H. & Wagner, A. (2006). *J. Synchrotron Rad.* **13**, 120.

Brück, S., Bauknecht, S., Ludescher, B., Goering, E. & Schütz, G. (2008). *Rev. Sci. Instrum.* **79**, 083109.

Bunk, O. & Nielsen, M. M. (2004). *J. Appl. Cryst.* **37**, 216.

Busing, W. R. & Levy, H. A. (1967). *Acta Cryst.* **22**, 457.

Ciatto, G., Chu, M. H., Fontaine, P., Aubert, N., Renevier, H. & Deschanvres, J. L. (2016). *Thin Solid Films*, **617**, 48.

Ciatto, G., Pettinari, G. & Polimeni, A. (2018). *J. Appl. Phys.* **124**, 165709.

Desjardins, K., Pomorski, M. & Morse, J. (2014). *J. Synchrotron Rad.* **21**, 1217.

Dyadkin, V., Pattison, P., Dmitriev, V. & Chernyshov, D. (2016). *J. Synchrotron Rad.* **23**, 825.

Einfeld, D. (2014). *Synchrotron Radiation News*, **27**, 4.

Enquist, H., Jurgilaitis, A., Jarnac, A., Bengtsson, A. U. J., Burza, M., Curbis, F., Disch, C., Ekström, J. C., Harb, M., Isaksson, L., Kotur, M., Kroon, D., Lindau, F., Mansten, E., Nygaard, J., Persson, A. I. H., Pham, V., Rissi, M., Thorin, S., Tu, C.-M., Wallén, E., Wang, X., Werin, S. & Larsson, J. (2018). *J. Synchrotron Rad*, **25**, 570.

Feidenhans'l, R. (1989). *Surf. Sci. Rep.* **10**, 105.

Fontaine, P., Ciatto, G., Aubert, N. & Goldmann, M. (2014). *Sci. Adv. Mater.* **6**, 2312.

Fouchet, A., Allain, M., Bérini, B., Popova, E., Janolin, P.-E., Guiblin, N., Chikoidze, E., Scola, J., Hrabovsky, D., Dumont, Y. & Keller, N. (2016). *Mater. Sci. Eng. B*, **212**, 7.

Fouchet, A., Rault, J. E., Allain, M., Bérini, B., Rueff, J.-P., Dumont, Y. & Keller, N. (2018). *J. Appl. Phys.* **123**, 055302.

Fuchs, M. R., Pradervand, C., Thominet, V., Schneider, R., Panepucci, E., Grunder, M., Gabadinho, J., Dworkowski, F. S. N., Tomizaki, T., Schneider, J., Mayer, A., Curtin, A., Olieric, V., Frommherz, U., Kotrle, G., Welte, J., Wang, X., Maag, S., Schulze-Briese, C. & Wang, M. (2014). *J. Synchrotron Rad.* **21**, 340.

Fuoss, P. H. & Robinson, I. K. (1984). *Nucl. Instrum. Methods Phys. Res.* **222**, 171.

Grabis, J., Nefedov, A. & Zabel, H. (2003). *Rev. Sci. Instrum.* **74**, 4048.

Gu, M., Wolf, S. A. & Lu, J. W. (2014). *Adv. Mater. Interfaces*, **1**, 1300126.

Hawthorn, D. G., He, F., Venema, L., Davis, H., Achkar, A. J., Zhang, J., Sutarto, R., Wadati, H., Radi, A., Wilson, T., Wright, G., Shen, K. M., Geck, J., Zhang, H., Nov V. & Sawatzky, G. A. (2011). *Rev. Sci. Instrum.* **82**, 073104.

Hodeau, J.-L., Favre-Nicolin, V., Bos, S., Renevier, H., Lorenzo, E. & Berar, J.-F. (2001). *Chem. Rev.* **101**(6), 1843–1868.

Huang, Z., Bartels, M., Xu, R., Osterho, M., Kalbfleisch, S., Sprung, M., Suzuki, A., Takahashi, Y., Blanton, T. N., Salditt, T. & Miao, J. (2015). *Nat. Mater.* **14**, 691.

Jaouen, N., Tonnerre, J.-M., Kapoujian, G., Taunier, P., Roux, J.-P., Raoux, D. & Sirotti, F. (2004). *J. Synchrotron Rad.* **11**, 353.

Ju, G., Highland, M. J., Yanguas-Gil, A., Thompson, C., Eastman, J. A., Zhou, H., Brennan, S. M., Stephenson, G. B. & Fuoss, P. H. (2017). *Rev. Sci. Instrum.* **88**, 035113.

Kitegi, C., Briquez, F., Couprie, M.-E., El Ajjouri, T., Filhol, J.-M., Tavakoli, T. & Vétéran, J. (2010). *Proceedings of IPAC'10, Kyoto, Japan*, p. 3099.

Lee, J. H., Tung, I. C., Chang, S.-H., Bhattacharya, A., Fong, D. D., Freeland, J. W. & Hong, H. (2016). *Rev. Sci. Instrum.* **87**, 013901.

Létoublon, A., Favre-Nicolin, V., Renevier, H., Proietti, M. G., Monat, C., Gendry, M., Marty, O. & Priester, C. (2004). *Phys. Rev. Lett.* **92**, 186101.

Lohmeier, M. & Vlieg, E. (1993). *J. Appl. Cryst.* **26**, 706.

Malibert, C., Dkhil, B., Kiat, J., Durand, D., Bérar, J. F. & Spasojevic, A. (1997). *J. Physics C: Condensed Matter*, **9**, 7485.

Mati Bloch, J. (1985). *J. Appl. Cryst.* **18**, 33.

McBride, E. E., Krygier, A., Ehnes, A., Galtier, E., Harmand, M., Konôpková, Z., Lee, H. J., Liermann, H.-P., Nagler, B., Pelka, A., Rödel, M., Schropp, A., Smith, R. F., Spindloe, C., Swift, D., Tavella, F., Toleikis, S., Tschentscher, T., Wark, J. S. & Higginbotham, A. (2018). *Nat. Phys.* **https://doi.org/10.1038/s41567-018-0290-x**.

Murphy, B. M., Greve, M., Runge, B., Koops, C. T., Elsen, A., Stettner, J., Seeck, O. H. & Magnussen, O. M. (2014). *J. Synchrotron Rad.* **21**, 45.

Nemoz, C., Ropars, V., Frit, P., Gontier, A., Drevet, P., Yu, J., Guerois, R., Pitois, A., Comte, A., Delteil, C., Barboule, N., Legrand, P., Baconnais, S., Yin, Y., Tadi, S., Barbet-Massin, E., Berger, I., Cam, E. L., Modesti, M., Rothenberg, E., Calsou, P. & Charbonnier, J. B. (2018). *Nat. Struct. Mol. Biol.* **25**, 971.

Nicklin, C., Arnold, T., Rawle, J. & Warne, A. (2016). *J. Synchrotron Rad.* **23**, 1245.

Nolle, D., Weigand, M., Audehm, P., Goering, E., Wiesemann, U., Wolter, C., Nolle, E. & Schütz, G. (2012). *Rev. Sci. Instrum.* **83**, 046112.

Nowak, D. E., Blasini, D. R., Vodnick, A. M., Blank, B., Tate, M. W., Deyhim, A., Smilgies, D.-M., Abru¯a, H., Gruner, S. M. & Baker, S. P. (2006). *Rev. Sci. Instrum.* **77**, 113301.

Pfeifer, M. A., Williams, G. J., Vartanyants, I. A., Harder, R. & Robinson, I. K. (2006). *Nature*, **442**, 63.

Pietsch, U., Holý, V. & Baumbach, T. (2004). *High-Resolution X-Ray Scattering. From Thin Films to Lateral Nanostructures*. Springer Verlag.

Seeck, O. H., Deiter, C., Pflaum, K., Bertam, F., Beerlink, A., Franz, H., Horbach, J., Schulte-Schrepping, H., Murphy, B. M., Greve, M. & Magnussen, O. (2012). *J. Synchrotron Rad.* **19**, 30.

Smilgies, D. M., Boudet, N., Struth, B. & Konovalov, O. (2005). *J. Synchrotron Rad.* **12**, 329.

Staub, U., Scagnoli, V., Bodenthin, Y., García-Fernández, M., Wetter, R., Mulders, A. M., Grimmer, H. & Horisberger, M. (2008). *J. Synchrotron Rad*, **15**, 469.

Strempfer, J., Francoual, S., Reuther, D., Shukla, D. K., Skaugen, A., Schulte-Schrepping, H., Kracht, T. & Franz, H. (2013). *J. Synchrotron Rad.* **20**, 541.

Takeuchi, T., Chainani, A., Takata, Y., Tanaka, Y., Oura, M., Tsubota, M., Senba, Y., Ohashi, H., Mochiku, T., Hirata, K. & Shin, S. (2009). *Rev. Sci. Instrum.* **80**, 023905.

Thorkildsen, G., Mathiesen, R. H. & Larsen, H. B. (1999). *J. Appl. Cryst.* **32**, 943.

Vlieg, E. (1998). *J. Appl. Cryst.* **31**, 198.

Yoshimatsu, K., Okabe, T., Kumigashira, H., Okamoto, S., Aizaki, S., Fujimori, A. & Oshima, M. (2010). *Phys. Rev. Lett.* **104**, 147601.

Zhang, S., Abiven, Y.-M., Blache, F., Corruble, D., Kheffafa, C. & Minolli, S. (2015). In *Proceedings, 15th International Conference on Accelerator and Large Experimental Physics Control Systems (ICALEPCS 2015): Melbourne, Australia, October 2015*, pp. 201–204.